Fluorescence-based mapping of condensate dielectric permittivity uncovers hydrophobicity-driven membrane interactions

E. Sabri[1], A. Mangiarotti[1,2,3] and R. Dimova[1]

[1]*Max Planck Institute of Colloids and Interfaces, Science Park Golm, 14476 Potsdam, Germany*
[2]*Centro de Investigaciones en Química Biológica de Córdoba (CIQUIBIC), CONICET, X5000HUA Córdoba, Argentina.*
[3]*Departamento de Química Biológica Ranwel Caputto, Facultad de Ciencias Químicas, Universidad Nacional de Córdoba, X5000HUA Córdoba, Argentina.*

ABSTRACT

Biomolecular condensates, essential for cellular organization, possess mesoscale properties largely governed by hydrophobicity, influencing molecule partitioning and material characteristics like viscosity, surface tension, and hydration. While hydrophobicity's role is recognized, its impact on membrane-condensate interactions remains unexplored. Here, we introduce a novel hyperspectral imaging approach, utilizing an environment-sensitive fluorescent dye and phasor analysis, to quantitatively map dielectric permittivity of both condensates and their environment with pixel resolution. This robust method reveals a surprisingly broad range of condensate permittivities, from oil-like to water-like. Importantly, we uncover that membrane affinity is not dictated by absolute condensate permittivity, but by the permittivity contrast with their surroundings. Indeed, membrane wetting affinity is found to scale linearly with this contrast, unveiling a unifying dielectric principle governing condensate-membrane interactions. Compatible with live-cell and *in vitro* imaging, this robust technique provides unprecedented insights into condensate biophysics and function and opens new avenues for studying biomolecular condensate biology.

INTRODUCTION

Biomolecular condensates form as a result of liquid-liquid phase separation (LLPS) and are key to intracellular organization. Examples of these phase-separated compartments include membraneless organelles such as stress granules[1], nucleoli[2], mitochondrial nucleoids[3] and nuclear speckles[4], which provide a dynamic and reversible means for cells to maintain homeostasis[1, 3, 4], adapt to stress[5-7] and regulate biochemical processes spatially and temporally[4, 8, 9]. The unique biophysical properties of condensates, such as viscosity[10-12], protein packing[13, 14], hydration[7, 15, 16], pH[17], surface tension[11] and electrostatic properties[18], set them apart from their surrounding environment and are crucial for their diverse functions. In particular, the hydrophobicity and perceived micropolarity of condensates, have recently emerged as readily measurable characteristics exhibiting strong correlations with each of these physicochemical parameters[9, 11, 19, 20].

While terms like "polarity"[21, 22] or "micropolarity"[11, 20, 23] are commonly encountered, their use can be misleading when referring to a material's dielectric properties. Dielectric permittivity, a continuum property, reflects not only the polarity of molecules (i.e. the degree of charge separation at the molecular scale) but critically, also their capacity to reorient in the presence of a transient electric field (e.g. originating from the transiently excited state of a dye dipole). A molecule can possess high intrinsic polarity (i.e., a pronounced charge separation) but if its rotational mobility is restricted, its contribution to the overall dielectric permittivity of the medium will be low, despite its high molecular polarity. This discrepancy arises because the effective screening of electric fields, fundamental to dielectric permittivity, requires molecular reorientation. Provided that water dipolar relaxation is the main factor of molecular reorientation in biological samples [24], we will primarily use the more suitable terms "hydrophobicity" or "dielectric permittivity". To ensure broad accessibility and to align with existing terminology in certain contexts, we will also employ "micropolarity" where appropriate, particularly when referencing established measurement paradigms.

Among the various techniques used to characterize condensates, fluorescence-based imaging has emerged as a powerful tool due to its sensitivity, non-invasiveness and high spatial and temporal resolution[11, 25-29]. From a fundamental perspective, fluorescence-based approaches quantify micropolarity on a dielectric permittivity scale, relying on the degree to which water molecules can redshift or quench the emission of environment sensitive dyes[11, 20-23]. Notably, these permittivity-sensitive dyes can detect how changes in protein sequence and interactions influence condensate properties *in vitro* and *in vivo*[11, 16, 30]. Given these insights, it is reasonable to predict that the dielectric permittivity of condensates is a key determinant in modulating their interactions with surrounding cellular components, such as membrane-bound organelles and the cytoskeleton. However, this critical aspect remains largely unexplored, primarily due to technical challenges associated with quantifying micropolarity, and establishing reliable calibration curves[11, 28]. Furthermore, while many environment-sensitive fluorescent probes exist[11, 20, 21, 23, 28, 31], their detection range is limited, failing to assess the sharp contrasts in dielectric properties which are hallmark features, endogenous to biological and bio-mimetic systems.

In this study, we introduce a robust, fluorescence-based method for quantifying the dielectric permittivity of biomolecular condensates and their surrounding environment. Our

approach utilizes 2-acetyl-6-(dimethylamino)naphthalene (ACDAN), a dipolar relaxation-sensitive dye[32, 33], widely used to probe intracellular water activity[34-36], macromolecular crowding[24] and membranous compartments[33, 37]. While ACDAN has previously been employed to infer dipolar relaxation in biomolecular condensates, these applications relied on inherently qualitative, arbitrary unitless scales. Here, we overcome this limitation by proposing a rigorous framework to establish a quantitative and broadband estimation of condensate dielectric permittivity based on the spectral response of ACDAN. Importantly, our method enables a simultaneous measurement of the properties of both dense (condensate) and depleted (environment) phases.

Building on this, we investigated the hypothesis that condensates dielectric properties governs their interaction with cellular structures, particularly membranes. While prior work has shown that condensate-membrane affinity can depend on bilayer hydrophobicity, even with unchanged membrane surface composition[39], the direct role of condensate dielectric properties in these interactions remained unclear. Our results demonstrate a clear correlation between membrane binding and permittivity contrast between condensed depleted phases, revealing that dielectric mismatch directly governs condensate-membrane affinity. These findings thus establish the permittivity of the coexisting phases as key quantifiable parameters for understanding how biomolecular condensates interact with diverse cellular structures such as membrane-bound organelles and the cytoskeleton.

RESULTS

ACDAN hyperspectral imaging provides a highly sensitive readout of solvent permittivity

ACDAN fluorescence is highly sensitive to solvent micropolarity[24, 33-37] due to dipolar relaxation. Upon UV absorption, ACDAN's dipole moment increases, generating a local electric field. Surrounding solvent molecules reorient to align with this field, minimizing the dye-solvent system energy. This process creates a permittivity-dependent local surface charge around the solvated dye (Fig. 1a) and the solvent dipolar relaxation results in a redshift in fluorescence emission.

We tested ACDAN's spectral sensitivity using both spectrofluorimetry (see SI) and hyperspectral microscopy imaging. While spectrofluorimetry accurately determines solvent permittivity (Figs. S1-S3), it is restricted to bulk (cuvette) measurements and lacks spatial resolution, limiting its ability to resolve distinct dielectric properties in phase-separated (or heterogeneous) samples. Hyperspectral imaging overcomes this by measuring the emission spectrum at each pixel, thereby generating a spatially resolved spectral map (Fig. 1b). This enables the visualization of local permittivity variations across heterogeneous systems, including biomolecular condensates (illustrated in Fig. 1b and further demonstrated below).

To establish the calibration curve linking emission to dielectric permittivity, we analyzed the spectral data from images of homogeneous solutions of known permittivity using two approaches: Gaussian fitting and phasor plot analysis via the discrete Fourier transform[24].

For the Gaussian fitting approach, spectral data from each solution were averaged across all pixels to obtain a robust emission curve, which was then fitted with a Gaussian function (Fig. 1b sketch and Methods). Figure 1c presents the resulting calibration curve, linking ACDAN's maximum emission wavelength to solvent permittivity.

The phasor plot analysis involves computing the discretized Fourier transform of the dye emission spectrum and representing it as a point in a two-dimensional "phasor plot" (Fig. 1b, bottom right panel). The plot's modulation provides information on the broadness of the spectrum, which can be affected by, e.g., fluorescence quenching[40], while its phase reflects the emission spectrum center of mass, which directly depends on the permittivity of fluorophore microenvironment[24]. Thus, each spectrum is represented as a single point in phasor space. For a hyperspectral image stack, the set of spectra associated with all pixels yields a scatter plot (cloud) in the phasor space (as sketched in Fig. 1b). To map permittivity in a given system, we built a calibration curve by analyzing images of homogeneous solutions with known permittivity. This generated a reference phasor plot (Fig. S2), from which the phase was used to build a calibration curve Fig. 1d.

As proof of principle, Fig. 1c,d includes additional data for ethanol-water mixtures (blue circles), with dielectric constants estimated using the celebrated Maxwell-Garnett law of mixtures[41] (see Table S3 and Fig. S1c for spectra). We demonstrate in the SI that this approach yields equivalent results via spectrofluorimetry (Figs. S1-S3), and that a fit-free phasor representation in Fourier space also yields equivalent results to the Gaussian fit (see Figs. S1-S3).

The Lippert-Mataga equation[40] accurately models the calibration data, establishing the relationship between the maximum emission wavelength $\lambda_{\max}$ and solvent permittivity ε:

$$\frac{1}{\lambda_{\max}} \sim \mu_E \frac{(\mu_G - \mu_E)}{V_{dye} hc} f(\varepsilon) + \text{const}, \quad (1)$$

where μ_E and μ_G are the excited state and ground state dipole moments of the fluorophore, V_{dye} is the effective molecular volume of ACDAN, h is the Planck constant, c is the speed of light in vacuum, and $f(\varepsilon)$ is the generalized Debye function (see SI for full model description). While Eq. 1 accurately describes the hyperspectral imaging data (Fig. 1c,d), it shows discrepancies with the spectrofluorimetry data, for which an empirical logarithmic function provided a better fit (see Fig. S1d and SI text for discussion).

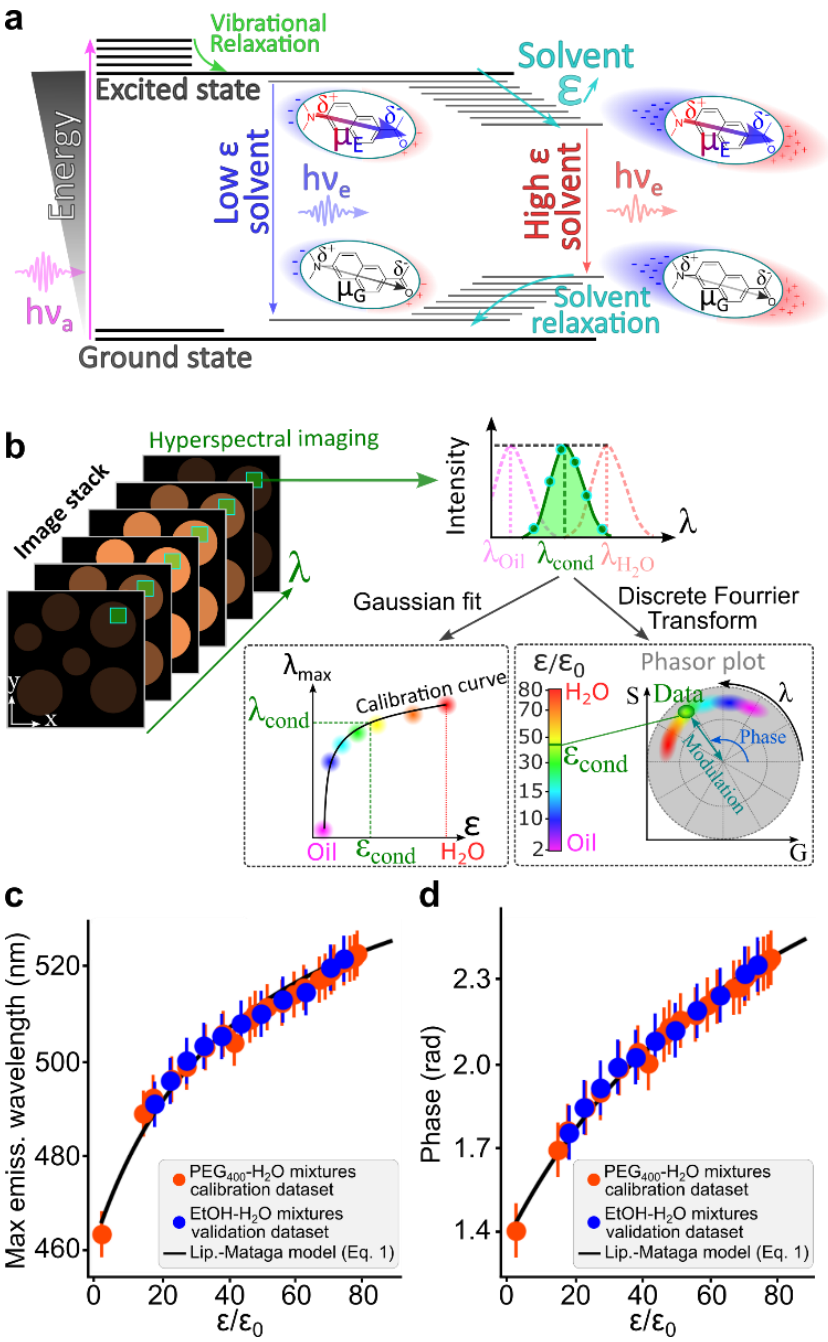

Figure 1: ACDAN hyperspectral imaging enables spatial mapping of dielectric permittivity with pixel resolution. (a) Perrin-Jablonsky diagram illustrating the dependence of ACDAN fluorescence on solvent permittivity. The sketch depicts the molecular structure of ACDAN, changes in its dipole moment due to photon absorption or emission and the solvent relaxation process. In low permittivity solvents, weak dipolar relaxation results in minimal redshift of the dye's fluorescence. Conversely, highly polar solvents lead to strong redshift due to enhanced solvent relaxation and a greater decrease in the energy gap for emission. $h\nu_a$ and $h\nu_e$ represent the absorption and emission energies, respectively. **(b)** Schematic representation of confocal hyperspectral imaging and analysis. A full emission spectrum is measured at each pixel from a stack of images acquired at different wavelengths (λ). The pixel permittivity (for either condensed or depleted phases) can be determined using two approaches: Gaussian fitting (bottom left) and phasor representation (bottom right). In the Gaussian fitting approach, the wavelength of maximum emission $\lambda_{\max}$ is plotted as a function of reported permittivity values to obtain a calibration curve (see panel c and text for details). In the phasor representation, the spectral information from an image is transformed into a point in 2D phasor space using the real (G) and imaginary (S) components of the discrete Fourier transform. The phase (reflecting the degree of

emission redshift) and modulation (reflecting spectrum broadness) of these points can be calibrated against reference permittivity values (graduated in the color bar) to map permittivity (see panel d and text for details). **(c, d)** Calibration data using the maximum emission wavelength of ACDAN obtained from a Gaussian fit of the spectrum (c) or the phase in the phasor plot (d) as a function of solvent dielectric constant (ε): Orange circles represent different PEG-400 solutions in water, with permittivity values from literature (referenced in Table S1). Blue circles represent ethanol-water mixtures, with dielectric constants calculated using the Maxwell-Garnett law of mixtures (see SI, Table S3 and Fig. S4b). The relation $\frac{\phi(\lambda_f-\lambda_0)}{2\pi}+\lambda_0=\lambda_{\max}$ with $\lambda_0=416\text{nm}$ and $\lambda_f=728\text{nm}$ was used to establish the link between the emission wavelength $\lambda_{\max}$, and the phase ϕ for which the Lippert-Mataga equation (Eq. 1, solid curve; fitting parameters given in Table S2) accurately describes the data.

Taken together, our results demonstrate that ACDAN emission provides a sensitive and broadband readout of dielectric permittivity ($2-80\varepsilon_0$). This robust sensitivity is conserved across different solvent chemistries and independent of the instrumental platform (microscopy or spectrofluorimetry).

In the following, we employ the microscopy-based phasor approach to resolve biomolecular condensates permittivity (calibration detailed in Fig. S2). We chose this method for two key reasons: first, its lack of requirement for an analytical fit function, especially relevant for probes with complex emission spectra (e.g. Laurdan[16] or multifunctional florescent probes[23, 42]) that are not accurately described by Gaussian models; second, it exhibits superior accuracy, with a maximum error of 8% compared to 13% for Gaussian fitting (Table S3).

Hyperspectral imaging allows determination of biomolecular condensates permittivity

To evaluate condensate permittivity, we analyzed six different systems undergoing distinct types of LLPS: (i) segregative LLPS in polyethylene-glycol (PEG)–bovine serum albumin (BSA), and PEG–dextran solutions, (ii) self-coacervation in myelin basic protein (MBP) and soy-plant based glycinin condensates, and (iii) complex coacervation in adenosine triphosphate (ATP)–polydiallyldimethylammonium chloride (PDDA), and oligopeptides-based condensates made of poly-lysine (K)–poly-aspartic acid (D) (K_{10}-D_{10}) and poly-arginine (R)–poly-aspartic acid (D) (R_{10}-D_{10}). Among these, the PEG-dextran, glycinin, and PEG-BSA systems were chosen for their cost-effectiveness and the feasibility of physically separating and analyzing their individual coexisting phases, facilitating more systematic characterization. The results of the phasor-based analysis of hyperspectral stacks for these systems are presented in Fig. 2.

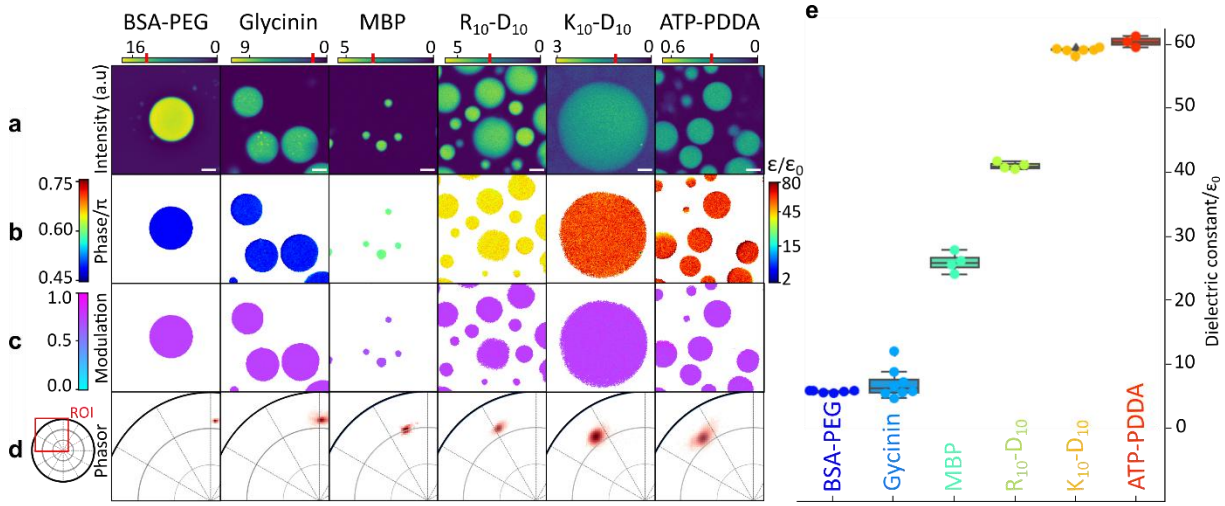

Figure 2: ACDAN hyperspectral imaging enables the broad-range determination of biomolecular condensate dense phase permittivity. (a) Representative mean intensity images of various biomolecular condensate systems, as labeled. Upper color bars indicate fluorescence intensity (arbitrary units), with red marks denoting the pixel exclusion threshold. Scale bars: 5µm. **(b)** Local dielectric permittivity maps (right color bar) derived from the spectral phase (left color bar). The spectral phase, which roughly reflects the emission maximum (see Fig. 1b and Methods), is translated into permittivity values using the microscopy-based phasor calibration curve (Fig. 1d). **(c)** Maps of spectral modulation (left color bar), reflecting spectrum broadness (Fig. 1b, Methods) showing only minor differences across condensate systems. **(d)** Phasor plot representation of the spectral information. Each dot represents the phase and modulation of an individual pixel from the image stacks in (a). The left inset highlights the region of interest (ROI) covering the experimental permittivity range (from $2\varepsilon_0$ to $80\varepsilon_0$). The spread of the pixel cloud illustrates the measurement error. **(e)** Dielectric permittivity values for all imaged condensate systems span a surprisingly broad range from ~$5\varepsilon_0$ (comparable to oil-like environments) to ~$60\varepsilon_0$ (closer to water). Each dot represents data from a stack of images. Box plots indicate mean±SD (BSA-PEG and K_{10}-D_{10}: n=6, glycinin: n=8, ATP-PDDA: n=3, R_{10}-D_{10} and MBP: n=4); see Fig. S4 for additional statistical details and experimental conditions.

Panels (b-d) of Fig. 2 were produced by applying a minimal intensity threshold to filter the highest intensity portion of the data in panel (a). This procedure distinguished condensates already settled at the bottom of the imaging chamber (highest mean signal) from those sedimenting into the observation plane during acquisition (moderate to low mean signal). The latter exhibited artificially elevated permittivity due to the absence of shorter-wavelength spectral components and were therefore excluded from the analysis as indicated in Fig. 2a.

Figure 2b-c shows that while phase values (related to emission maximum, Fig. S2), and thus permittivity (Fig. 2b), vary significantly among condensate systems, the modulation (related to spectra broadness, Fig. S2) only slightly decreases with increasing permittivity (Fig. 2c). This observation is further evident in Fig. 2d and consistent with the expected fluorescence quenching effect associated with dipolar relaxation[40]. The spread of the pixel cloud in Fig. 2d visually illustrates measurement error, which is inversely proportional to the signal-to-noise ratio.

Averaging the phase values and converting them to permittivity yields Fig. 2e (additional statistical details in Fig. S4). The data reveal a remarkably broad range of dielectric constants across different condensates, from values as low as ~$5\varepsilon_0$ (typical of oil-like environments) to as high as ~$60\varepsilon_0$ (approaching that of water), highlighting substantial variability in condensate hydrophobicity. Importantly, the weak correlation between the type of interaction driving LLPS

and condensate permittivity (Fig. 2e) suggests that condensate dielectric properties cannot be predicted solely based on the chemical nature of components or the LLPS mechanism. A striking example is the comparison between K_{10}-D_{10} and R_{10}-D_{10} condensates: despite the small difference of only four atoms between the structures of lysin and arginine, the permittivities differ drastically, i.e. by ~$20\varepsilon_0$ (Fig. 2e).

Determining condensate permittivity provides a fingerprint of its phase-state

Changes in macromolecules concentration within either the dense or depleted phase modulate protein hydration and water activity, thereby altering the permittivity contrast between the two phases[2, 11, 43]. Thermodynamically, such shifts reflect changes in the system position on its phase diagram[44]. From this perspective, measuring the permittivity contrast between two coexisting phases provides a direct readout of a mixture's phase state, enabling the estimation of key parameters like interfacial tension[45]. This is particularly important when investigating the fundamental origin of biologically relevant phenomena governed by interfacial tension, such as the wetting of membranes by biomolecular condensates[46, 47], which we discuss in the following section.

Hyperspectral imaging of ACDAN as applied here, allows for the simultaneous determination of the permittivity of both protein-poor and protein-rich phases. Figure 3 shows that the position in a mixture's phase diagram can be obtained by characterizing the permittivity of its coexisting phases.

Figure 3a,b shows how variations in the initial concentrations of PEG and dextran, schematically defined by points in the phase diagram of panel (a), translate into different permittivity values. Measurements of points (3-10) in Figs. 3a,b were performed by isolating each phase of the PEG-dextran aqueous two-phase system (ATPS); permittivity maps and initial concentrations are given in Fig. S5. Even a small increase in polymer concentrations (a few tens of percent) consistently results in lower permittivity, corroborating previous reports[49].

Figure 3c-g further emphasizes the generality of these trends, displaying data for glycinin and PEG-BSA systems. Figure 3c-e shows that different points in the glycinin phase diagram (Fig. 3b) correspond to markedly different permittivity values between homogeneous and phase separated states. Similarly, Fig. 3f shows that increasing the overall BSA concentration decreases the permittivity of the BSA-depleted phase, a trend quantified in Fig. 3g and compared to PEG-free BSA aqueous solutions.

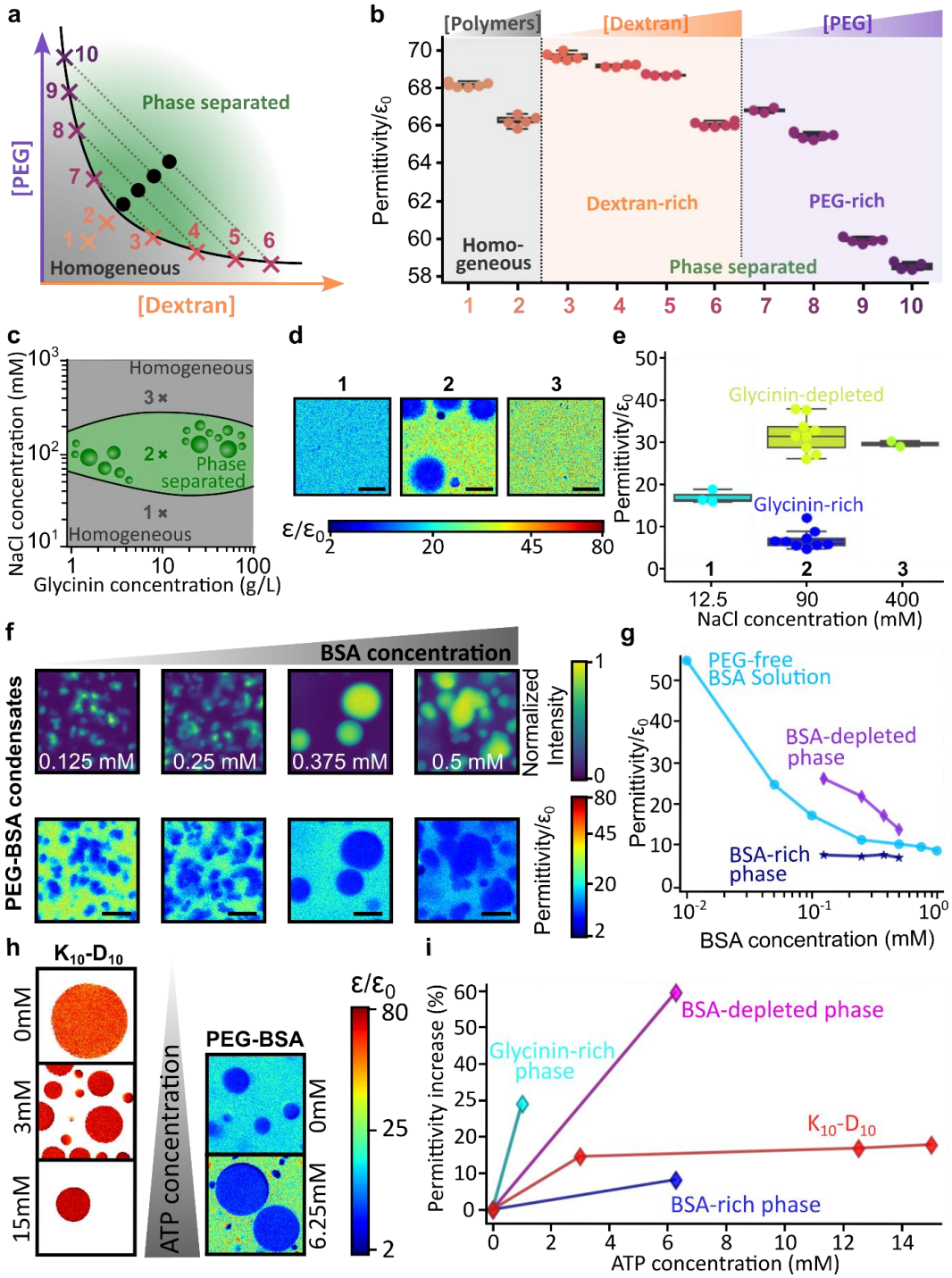

Figure 3: Hyperspectral imaging of condensate permittivity allows mapping of phase state changes. (a) Sketch of a PEG-dextran phase diagram, see [44] for experimental values. Points (1-2) represent homogeneous PEG-dextran mixtures. Black dots indicate phase-separated mixtures. Dotted tie lines connect coexisting phases, with crosses 3-6 along the binodal (black curve) indicating dextran-rich phase compositions and 7-10 denoting PEG-rich phase compositions. **(b)** Hyperspectral imaging-based permittivities of PEG-dextran mixtures corresponding to schematic points in (a), see Fig. S5 for exact compositions. **(b)** Hyperspectral imaging-based measurement of the permittivity of the PEG-dextran mixture compositions schematically presented in (a), see Fig. S5 for exact compositions. **(c)** Phase diagram of glycinin condensation as a function of protein and NaCl concentrations[48]. Grey regions indicate homogeneous mixtures and the green region denotes phase separation (condensate formation). Points 1, 2 and 3 correspond to NaCl concentrations of 12.5, 100, and 400 mM, respectively, at a constant protein concentration of 10 g/L. **(d)** Example permittivity maps for glycinin solutions at three NaCl concentrations indicated in (c). The color bar represents rescaled permittivity. Scale bars: 10µm.

(e) Quantified permittivity of all phases at points 1, 2 and 3 in (c,d). **(f)** Effect of BSA concentration on the permittivity of PEG-BSA condensate systems. Top: average intensity projections of hyperspectral stacks for different initial BSA concentrations (indicated in white). Bottom: corresponding permittivity maps of the same regions, showing a gradual decrease in the depleted phase permittivity with increasing protein concentration. Scale bars: 10µm. **(g)** Increasing the total BSA concentration lowers the permittivity of homogeneous protein solutions in water (blue circles) and BSA-depleted phase (diamonds), but has no significant effect on the PEG-BSA condensates (stars). **(h)** Permittivity maps illustrating the effect of increasing ATP concentration on K_{10}-D_{10} and BSA-PEG condensates. Each frame represents a 36.9×36.9µm^2 sample area. The color bar (logarithmic scale) indicates permittivity. Left: permittivity maps of K_{10}-D_{10} condensates showing increasing permittivity with ATP concentration. Right: permittivity maps of BSA-PEG condensates (10wt% PEG, 0.375 mM BSA) demonstrating a similar trend. **(i)** Impact of ATP concentration on the permittivity of K_{10}-D_{10}, and BSA-PEG (condensates shown in h) and glycinin condensates (10 g/L total protein in 100 mM NaCl). Permittivity values in the absence of ATP are given in Fig. 2.

Given that BSA is the main hydrophobic component of the mixture, this representation allows a qualitative estimate of BSA concentration in different regions of the phase-separated system (the permittivity map of the BSA solutions used in Fig. 3g is provided in Fig. S6). For example, the BSA-depleted phase at a total BSA concentration of 0.125 mM exhibits a permittivity similar to that of a 0.05 mM BSA solution, suggesting that the latter closely approximates the concentration of the depleted phase. Conversely, the permittivity of the BSA-rich phase suggests a BSA concentration close to 10 mM. Figure S7 presents a similar comparison for glycinin, contrasting salt-free glycinin solutions with the two phases of its phase-separated counterpart (i.e., point 2 in Fig. 3c-e). Since enzymatic activity requires a highly hydrophilic environment for a hydrogen-bonded water network to form at the enzyme surface preserving biologically active[50, 51], the results of Fig. 3 align with reports of decreased enzymatic activity in the condensed phase of PEG-BSA mixtures compared to homogeneous BSA solutions of similar overall concentrations[52].

To further assess the sensitivity of our method to subtle physicochemical changes, we investigated the effects of ATP as a hydrotrope – a small molecule known to enhance protein solubility and hydration [38, 53, 54] – and examined its effect on the dielectric permittivity of various condensate systems. Figure 3h,i shows how increasing ATP concentration significantly alters the permittivity of different condensate systems. These results underscore the sensitivity of this method sensitivity in detecting subtle variations in hydration and microenvironment within both condensed and depleted phases. Specifically, adding just a small amount of ATP progressively increases the permittivity of glycinin and K_{10}-D_{10} condensates by approximately 25% and 15%, respectively (Fig. 3i). Similar trends are observed in the BSA-PEG system, where the depleted phase permittivity increases by 60% upon addition of 6.25 mM ATP, compared to a modest 8% increase for the condensed phase. These differential responses suggest that ATP shifts the system's position on its phase diagram by selectively altering the hydration and dielectric permittivity of the coexisting phases.

Overall, these findings emphasize that quantifying the permittivity of both condensate and its surrounding environment allows for the characterization of a given system's position in its phase diagram. Furthermore, an estimation of the composition of each coexisting phase can be made and fine variations in phase behavior and hydration captured.

Permittivity contrast between dense and depleted phases governs condensate-membrane interaction

Building on the hypothesis that condensate hydrophobicity governs interactions with cellular structures like membranes, we investigated whether dielectric properties directly influence condensate-membrane affinity. Previous work shows that condensate-membrane interactions vary with bilayer hydrophobicity, modulated by, for example, lipid tails saturation, even when membrane surface chemistry (lipid headgroups) remains unchanged[39]. This intuitively suggests that condensate hydrophobicity, quantified through permittivity, may govern this interaction.

Upon contacting a membrane, condensates undergo a wetting transition reflecting the strength of their interaction[57]. This leads to mutual reshaping of both the membrane and the condensate[47], where the resulting equilibrium morphology directly reflects the interaction affinity. Figure 4a presents an example of such a morphology, well-described by the theoretical framework introduced in ref. [47].

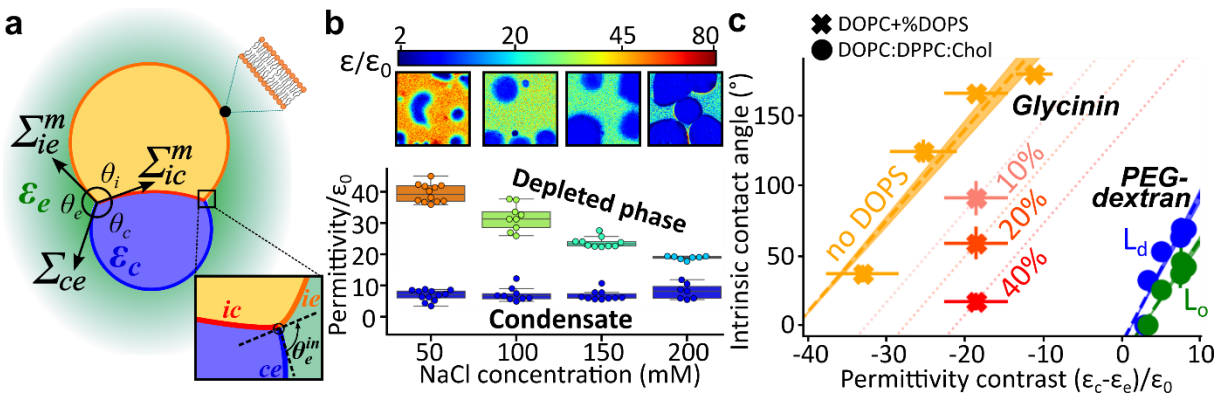

Figure 4: Membrane wetting by condensates is modulated by the permittivity contrast between coexisting phases. (a) Schematic illustration of a vesicle (yellow) wetted by the condensate (blue, permittivity ε_c) and surrounded by the depleted phase (light green, permittivity ε_e). Apparent contact angles facing the vesicle interior (θ_i), the external phase (θ_e), and the condensate (θ_c), define the system equilibrium morphology. These angles reflect a balance of interfacial forces at the three-phase contact line (black circle): the condensate interfacial tension Σ_{ce}, and the mechanical tensions of the two membrane segments in contact with the depleted condensate-free phase (Σ_{ie}^m, orange) and condensate phase (Σ_{ic}^m, red). At the nanometer scale, the membrane is smoothly curved (inset), and wetting is described by the intrinsic contact angle $\theta_e^{in} = \arccos\left(\frac{\sin\theta_e - \sin\theta_c}{\sin\theta_i}\right)$ [47], see Methods. **(b)** Hyperspectral permittivity maps of glycinin condensates at increasing NaCl concentrations. Top: dielectric maps of fields of view (36.9×36.9μm^2). The color bar represents the logarithmic permittivity scale. Bottom: boxplot showing that increasing salt primarily lowers the permittivity of the condensate-free (depleted) phase, while the condensate phase remains relatively unaffected. **(c)** The intrinsic contact angle θ_e^{in}, describing condensate-membrane affinity, increases linearly with the permittivity contrast ($\varepsilon_c - \varepsilon_e$), indicating that stronger permittivity differences enhance membrane wetting by the condensate. All experimental datasets were fitted with a linear function (dashed lines). Crosses display θ_e^{in} data from ref. [47] for glycinin condensates interacting with DOPC:DOPS membranes at various NaCl concentrations (pure DOPC, orange), and for 100 mM NaCl but different charged lipid content (10, 20 and 40 mol% DOPS, respectively shown in rose, vermilion and red); the respective permittivity contrast $\varepsilon_c - \varepsilon_e$ is from panel (b). Dotted lines passing through data points for DOPS-doped membranes have the same slope as the charge-free membrane and serve as guides to the eye. Circles show θ_e^{in} data from ref. [44] for PEG-dextran ATPS droplets at different polymer concentrations in contact with either liquid-disordered (Ld, DOPC:DPPC:Chol, 64:15:21, blue) or liquid-ordered (Lo, 13:44:43, green) membranes. The corresponding permittivity contrasts are interpolated from Fig. 3b.

The force balance between the tensions of the wetted (Σ_{ic}^{m}) and bare (Σ_{ie}^{m}) membrane segments and the condensate interfacial tension (Σ_{ce}) [47] (see Methods) shapes the vesicle-condensate couple into an axisymmetric system characterized by three apparent contact angles ($\theta_i, \theta_c, \theta_e$) (Fig. 4a and Methods). At the nanometer scale, the membrane at the three-phase contact line (black circle in Fig. 4a) is smoothly curved and wetting is described by the intrinsic contact angle θ_e^{in}. This geometry-independent material parameter encodes the membrane preference for either the protein-rich (condensed) or protein-poor (depleted) phase[47].

While θ_e^{in} has been shown to vary with salt, polymer or protein concentration[16, 44, 57], membrane charge[16] and lipid composition[39], the fundamental basis underlying these variations remains unclear. Intuitively, one might expect that a condensate with a permittivity similar to that of the membrane would exhibit stronger affinity. However, the intrinsic contact angle reflects not the absolute affinity of one phase for the membrane, but rather the relative affinities of the two coexisting aqueous phases, see Methods. Because the sum of the contact angles opening toward each phase must equal 180° (see inset in Fig. 4a), a change in membrane preference for one phase necessarily implies a corresponding change for the other. Therefore, condensate-membrane affinity, as quantified by θ_e^{in}, must be governed not by the condensate permittivity alone, but by the contrast between the condensed and depleted phases. This deduction is supported by Fig. 4b showing constant condensate permittivity for conditions where θ_e^{in} was reported to vary[47]. Thus, we hypothesized that variations in θ_e^{in} originate from differences in hydrophobicity between the condensed and depleted phases, precisely captured by their permittivity contrast.

As a first step to test this hypothesis, we quantified the permittivities of coexisting phases in heterogeneous glycinin solutions and PEG-dextran ATPS. While the permittivity of the glycinin-depleted phase exhibited decrease markedly with increasing salt concentration, the condensed phase remained unaffected (Fig. 4b). This led to a monotonic decrease in the permittivity contrast ($\varepsilon_c - \varepsilon_e$). For PEG-dextran mixtures (Fig. 3b), increasing polymer concentration caused both phases to become less polar, with a stronger permittivity drop in the PEG-rich phase compared to the dextran-rich droplet phase, resulting in an increase in permittivity contrast ($\varepsilon_c - \varepsilon_e$) with increasing overall polymer concentration. These trends show that permittivity contrast can be precisely tuned by modulating external variables such as ionic strength or polymer concentration.

We then examined whether this permittivity contrast correlates with condensate–membrane wetting. Figure 4c reveals a linear dependence of the intrinsic contact angle on $\varepsilon_c - \varepsilon_e$ across independent θ_e^{in} datasets for various membrane types and condensate systems taken from refs. [44, 47]. This universal linear correlation suggests a fundamental biophysical mechanism where the membrane preference between condensed and depleted phases depends primarily on their permittivity contrast.

In first approximation, this trend could be understood considering the membrane adhesion free energies to the two aqueous phases: W_{mc} for the condensate and W_{me} for the depleted phase (see Methods). Assuming each adhesion energy depends on the permittivity contrast between the membrane and the respective aqueous phase, ($\varepsilon_c - \varepsilon_m$) and ($\varepsilon_c - \varepsilon_m$), the affinity contrast $W = W_{mc} - W_{me}$ becomes proportional to $\varepsilon_c - \varepsilon_e$. Thus, the intrinsic contact angle, which encodes this affinity contrast, naturally reflects the dielectric difference between the two phases.

As we see in Fig. 4c, the slope and offset of this linear relation are influenced by the membrane lipid composition, surface charge, and the specific condensate system.

Overall, these results underscore the crucial role of permittivity contrasts in modulating surface affinities between membranous compartments and protein-rich droplets. They highlight that condensate-membrane interactions cannot be understood by considering the dielectric properties of the condensates alone; rather, it is the permittivity difference between the condensed and depleted phases that governs affinity. Significantly, the ability of hydrotropes like ATP to differentially modulate the permittivity of coexisting phases (Fig. 3h,i) offers a mechanism to precisely tune condensate recruitment or repulsion from cellular membranes.

These findings call for systematic assessment of both phases when probing condensate interactions with biological materials. Hyperspectral permittivity mapping thus emerges as a powerful approach for understanding the physical principles that guide biomolecular condensation and its functional coupling to membrane systems.

DISCUSSION

The dielectric permittivity of biomolecular condensates is increasingly recognized as a key parameter linking their biophysical properties to physiological function[2, 7, 11]. Notably, permittivity differences between immiscible biopolymer phases govern their interfacial surface tension[2, 11, 28], which in turn stabilizes complex core-shell architectures in nuclear organelles[2]. This interdependence fundamentally arises from a water activity gradient that imposes an entropic penalty on interfacial water molecules[43, 58, 59]. Consequently, LLPS enables cells to locally regulate intracellular water activity and internal permittivity, acting as a feedback mechanism to buffer against osmotic or thermal stress[7, 60].

Our study introduces a powerful hyperspectral imaging approach using the environment-sensitive fluorophore ACDAN to quantitatively map local dielectric permittivity of biomolecular condensates and their surrounding environment. This parameter, while crucial for understanding phase behavior, has remained experimentally elusive, especially in complex, heterogeneous systems where high resolution and dynamic range are essential. Our method provides robust, broadband measurements (2–80ε_0) independent of solvent chemistry or instrumental platform. Notably, we reveal a surprisingly wide range of dielectric permittivities across different condensates, spanning from oil-like (~5ε_0) to water-like (~60ε_0), see Fig. 2e, highlighting substantial and unexpected variability in their hydrophobicity. Importantly, we find that condensate permittivity is not solely dictated by the type of underlying LLPS interactions (Figs. 2,3), but is rather strongly influenced by the protein-to-water ratio within the condensed phase. To confirm this, we performed Raman spectroscopy measurements (Fig. S8), which revealed that higher-permittivity condensates like K_{10}-D_{10} contain more water relative to peptide compared to condensates characterized by lower permittivity like R_{10}-D_{10} (Fig. 2).

Beyond hydration and phase behavior, our high-resolution approach, which allows simultaneous measurement of both condensed and depleted phases, provides important new insights into the interactions of condensates with membranes. We find that it is not the absolute permittivity of condensates, but rather the permittivity contrast with their environment, that is the central parameter controlling interactions with lipid membranes. A key result of our study is the discovery of a universal linear relationship between the intrinsic contact angle, which characterizes membrane-condensate affinity, and the permittivity contrast between coexisting

condensed and their environment (Fig. 4c). While many studies focus solely on the properties of the condensate phase, our findings underscore the critical importance of also characterizing the protein-poor condensate environment. We established a direct link between the dielectric properties of phase-separated systems and their interfacial interactions.

Given that the hydrophobic core of lipid membranes exhibits a low permittivity (comparable to oils), condensates with inherently low dielectric permittivity are likely to exhibit greater affinity to membranes. At comparable permittivity contrasts, we speculate that such condensates, like glycinin and BSA-PEG (Fig. 2e), will display enhanced membrane wetting compared to more hydrophilic, high-permittivity condensates, such as K_{10}-D_{10}, ATP-PDDA and the dextran-rich phase in PEG-dextran ATPS (Figs. 2e and 3b). The membrane surface charge further modulates this interaction: achieving the same intrinsic contact angle on charged membranes requires a higher permittivity contrast than on neutral membranes (Fig. 4c). Similarly, more ordered (and presumably more hydrophobic due to higher lipid packing) membranes demand larger permittivity contrasts to reach comparable wetting, likely due to their lower intrinsic permittivity.

We also propose that lower-permittivity condensates may preferentially stabilize hydrophobic membrane defects like pores, a property with potential relevance for cellular membrane repair. In this context, condensates can act as plugs for transient membrane pores, helping to stabilize and reseal damaged membrane organelles[5, 65]. Condensates with lower permittivity may likely allow better integration with the hydrophobic membrane environment, facilitating pore sealing and restoring membrane integrity.

Beyond these fundamental insights, our method provides a sensitive fingerprint of phase-separated systems' thermodynamic state (Fig. 3), allowing the quantification of subtle changes induced by hydrotropes like ATP (Fig. 3h,i). Considering ATP's relevance in cellular function, our results suggest that it not only influences protein solubility[37, 38] but also acts as a key modulator of condensate interactions with other cellular components, by affecting permittivity contrast.

Overall, our results underscore the utility of this method in mapping fine variations in phase behavior, composition, and dielectric properties with high spatial resolution and across diverse biomolecular condensate systems. We believe these findings significantly advance the physical framework for understanding the interplay between electrostatics, phase separation, and biological function in complex and heterogeneous biomolecular systems and in understanding condensate interactions. Given the accessibility of hyperspectral imaging on commercial confocal microscopes[66], the method is poised to become a valuable tool for studying dynamic intracellular environments and advancing the understanding of biomolecular phase transitions in health and disease. The approach paves the way for new investigations into the physicochemical mechanisms underlying condensate function, aging and liquid-to-solid transitions associated with neurodegenerative pathologies[30, 67].

METHODS

Materials

6-acetyl-2-dimethylaminonaphthalene (ACDAN) was purchased from Santa Cruz Biotechnology (USA). Polydiallyldimethylammonium chloride (PDDA, 200-350 kDa, 20 wt% solution in water), adenosine triphosphate (ATP) and sodium hydroxide (NaOH) were obtained

from Sigma-Aldrich (Missouri, USA). Poly(ethylene glycol) (PEG 8000, Mw 8kg/mol and PEG 400, Mw 4kg/mol) and dextran from Leuconostoc mesenteroides (molecular weight between 400 kDa and 500 kDa) were purchased from Sigma-Aldrich. The oligopeptides, poly-L-lysine hydrochloride (degree of polymerization, n = 10; K_{10}), poly and poly-L-aspartic acid sodium salt (n=10; D_{10}) were purchased from Alamanda Polymers (AL, USA) and used without further purification (≥95%). BSA (≥98% purity, 66kg/mol), MBP bovine (≥90%), 1,4-Dioxane, Anisol (99%), 1-Hexanol and 1-Butanol (99.9%) were purchased from Sigma-Aldrich. Mineral oil was purchased from Carl Roth GmbH. Ethanol absolute was purchased from VWR chemicals BDH. Phosphate buffered saline (PBS) pH 7.2 was purchased from Thermofisher. Polyvinyl alcohol (PVA, Mw 145000kg/mol) was purchased from Merck (Darmstadt, Germany). All solutions were prepared using ultrapure water from SG water purification system (Ultrapure Integra UV plus, SG Wasseraufbereitung) with a resistivity of 18.2 MΩ cm.

Condensate formation and labelling

Coverslips for confocal microscopy (26×56 mm, Waldemar Knittel Glasbearbeitungs GmbH, Germany) were washed with ethanol and water, then passivated with a 10 mg/mL BSA solution and an aliquot of 10µL of condensates suspension was placed on the coverslip before imaging.

PDDA-ATP condensates: Phase separated droplets were formed by gently mixing aliquots of stock solutions of ATP and PDDA (in this order) with ACDAN in pure water to a final volume of 10 µL. The final concentration of each component was as follows: 14.8 mM ATP, 4.9 mM PDDA, 10µM ACDAN.

Glycinin condensates: Freeze-dried glycinin was a gift from Dr. Nannan Chen. The purification is detailed in ref [48]. A 20 mg/mL glycinin solution at pH 7 was freshly prepared in ultrapure water and filtered with 0.45 µm filters to remove any insoluble materials. To form the condensates, the desired volume of the glycinin solution was mixed with the same volume of a NaCl solution of twice the desired final concentration. In this manner, the final protein concentration was 10 mg/mL[48]. The final concentration of ACDAN was 5µM.

K_{10}-D_{10} and R_{10}-D_{10} condensates: Phase separated droplets were formed by gently mixing aliquots of stock solutions of D_{10} and K_{10} or R_{10} (in this order) with ACDAN in pure water to a final volume of 10 µL. The final concentration of each component was as follows: 2.5 mM D_{10}, 2.5 mM K_{10} or R_{10}, 15µM ACDAN.

PEG-BSA condensates: Phase separated droplets were formed by gently mixing aliquots (via pipetting and releasing 3 times the total volume) in a 1:1 ratio of stock solutions of 20% PEG-8000 in PBS with 30µM ACDAN with BSA dissolved in PBS at half the desired concentration and to a final volume of 10 µL.

PEG-Dextran condensates: A polymer solution in composed of the desired weight fractions of PEG and dextran were prepared and left, when relevant, for 2 days to completely phase separate and equilibrate. ACDAN was then added to each phase to reach a final concentration of 25µM of ACDAN.

MBP condensates: MBP condensates were prepared by following the procedure described in [68]. Briefly, a 5mg/mL solution of MBP dissolved in water was mixed with a 20mM NaOH solution of 10µM ACDAN in a 1:1 ratio.

Confocal microscopy and hyperspectral imaging

Hyperspectral images were acquired using a confocal Leica SP8 FALCON microscope equipped with a 63×, 1.2 NA water immersion objective (Leica, Mannheim, Germany). The microscope was coupled to a pulsed Ti:Sapphire laser MaiTai (SpectraPhysics, USA), with a repetition rate of 80 MHz. A two-photon wavelength of 780 nm was used for ACDAN excitation. Image acquisition was performed with a frame size of 512 × 512 pixels[16, 47] and a pixel size of 72 nm×72 nm using a Hyd SMD detector in standard mode. For hyperspectral imaging, the xyλ configuration of Leica SP8 was used, sequentially measuring in 32 channels with a bandwidth of 9.75 nm in the range from 416 to 728 nm. Some hyperspectral images were realigned using the ImageJ software and all hyperspectral stacks were processed by the SimFCS software developed at the Laboratory of Fluorescence Dynamics (available at https://www.lfd.uci.edu/globals/), and analyzed using Python code based in the PhasorPy library (available at https://www.phasorpy.org/).

Gaussian fit analysis

The Gaussian fit analysis of ACDAN hyperspectral imaging data consists in approximating the wavelength-intensity profile of ACDAN emission by a skewed Gaussian function of the form:

$$I(\lambda) = I_0\, \Psi\left(\frac{\lambda-\mu}{\sigma}\right)\, \Phi\left(\gamma\left(\frac{\lambda-\mu}{\sigma}\right)\right), \tag{M1}$$

$$\Psi\,(x) = \frac{1}{\sqrt{2\pi}}\exp\left(-\frac{x^2}{2}\right), \tag{M2}$$

$$\Phi(x) = \frac{1}{2}\left(1 + \mathrm{erf}\left(\frac{x}{\sqrt{2}}\right)\right), \tag{M3}$$

where Ψ, Φ, erf, λ, μ, σ, I_0 and γ respectively represent the normal distribution function, the cumulative distribution function, the error function, the wavelength, the mean wavelength, the mean deviation, the intensity scaling factor and the skewness factor. Data interpolation was performed based on computer programing script written in Python and based on the scipy library. The λ_{max} was then evaluated based on the position of the maximum of the fitted ACDAN emission curve and used as an input in the $\lambda - \varepsilon$ calibration curves presented in Figs. 1c and S1 in the main text.

Spectral phasor analysis

The spectral phasor analysis of ACDAN hyperspectral imaging data consists in calculating the real and imaginary components of the Fourier transform, respectively referred to as G and S, and using them as Cartesian coordinates on a 2D spectral phasor map. (G, S) are defined by the following expressions:

$$G = \frac{\int_{\lambda_0}^{\lambda_f} I(\lambda)\cos(\omega n(\lambda-\lambda_0))\mathrm{d}\lambda}{\int_{\lambda_0}^{\lambda_f} I(\lambda)\mathrm{d}\lambda}, \tag{M4}$$

$$S = \frac{\int_{\lambda_0}^{\lambda_f} I(\lambda)\sin(\omega n(\lambda-\lambda_0))\mathrm{d}\lambda}{\int_{\lambda_0}^{\lambda_f} I(\lambda)\mathrm{d}\lambda}, \tag{M5}$$

where $I(\lambda)$ for a particular pixel represents the intensity as a function of wavelength, measured in the interval $(\lambda_0; \lambda_f)$. This range depends on instrumental constraints and the type of detector used for the analysis, in our case 416–728 nm. Note that changing the detection range will necessarily results in a change of the relative positions of different points on the phasor plot;

therefore, the detection range must be conserved across all experiments in order to be able to compare measurements. The parameter n is the harmonic, i.e. the number of cycles of the trigonometric function that are fit in the wavelength range by means of the angular frequency ω:

$$\omega = \frac{2\pi}{(\lambda - \lambda_0)} \tag{M6}$$

When imaging with a microscope, we acquire a discrete number of spectral steps corresponding to the number of detection windows that cover the spectral range. For computational purposes, the spectral phasor transform is expressed as a discretized approximation of the continuous transform as:

$$G = \frac{\sum_c^{N_c} I(c)\cos(2\pi c/N_c)}{\sum_c^{N_c} I(c)}, \tag{M7}$$

$$S = \frac{\sum_c^{N_c} I(c)\sin(2\pi c/N_c)}{\sum_c^{N_c} I(c)}, \tag{M8}$$

where $I(c)$ is the pixel intensity at channel and c is the total number of channels. Conveniently, even if the total number of spectral acquisition channels is small (in our case 32), the coordinates S and G can be considered quasi-continuous, since the photon counts in each pixel and channel are high enough (~102) to allow a wide range of possible values of the coordinates S and G.

The spectral phasor approach obeys the rules of vector algebra, known as the linear combination of phasors. This property implies that a combination of two independent fluorescent species will appear on the phasor plot at a position that is a linear combination of the phasor positions of the two independent spectral species. The fraction of each component can be determined from the coefficients of the linear combination.

Note that the phase angle ϕ, and the modulation, M can be obtained through:

$$\phi = \arctan\left(\frac{S}{G}\right) \tag{M9}$$

$$M = \sqrt{S^2 + G^2} \tag{M10}$$

Data processing and spectral phasor analysis were performed by first converting the Image stacks into .r64 files using the SimFCS software developed at the Laboratory of Fluorescence Dynamics, available on the webpage (https://www.lfd.uci.edu/globals/), and further processed using Python programming code based on the PhasorPy library (https://www.phasorpy.org/).

Relating contact angles, mechanical parameters and permittivity contrast

This section is based on the theoretical framework derived in ref. [47]. Briefly, the contact angles in Fig. 4a, are related to the force balance between the different surface tensions of the three surface segments pulling along the membrane-condensate contact line. One of these tensions is the interfacial tension of the condensate-buffer interface Σ_{ce} (see Fig. 4a). The other two are the mechanical tensions of the two membrane segments in contact with the depleted phase (Σ_{ie}^m) and condensate (Σ_{ic}^m), given by[69]:

$$\Sigma_{ic}^m = \Sigma + W_{mc} \quad \text{and} \quad \Sigma_{ie}^m = \Sigma + W_{me} \tag{M11}$$

where Σ denotes the lateral stress within the membrane, whereas W_{mc} and W_{me} represent the adhesion free energies per unit area of the condensate and of the external depleted phase, relative to the interior solution[69]. The affinity contrast between the condensate and the external buffer is then given by[69] :

$$W = \Sigma_{ic}^m - \Sigma_{ie}^m = W_{mc} - W_{me} \tag{M12}$$

The geometry-dependent lateral membrane stress Σ drops out from the affinity contrast W which is negative if the membrane prefers the condensate phase over the external buffer, and positive otherwise. The force balance in Fig. 4a also implies the geometric relationships[69]

$$\frac{\Sigma_{ie}^{m}}{\Sigma_{ce}} = \frac{\sin\theta_c}{\sin\theta_i} \qquad \text{and} \; \frac{\Sigma_{ic}^{m}}{\Sigma_{ce}} = \frac{\sin\theta_e}{\sin\theta_i} \tag{M13}$$

between the surface tensions and the contact angles, as follows from the law of sines for the tension triangle in Fig. 4a. When we introduce Eqs. (M11) and take the difference of the two equations in Eq. (M13), for the affinity contrast W in Eq. (M12) we arrive at

$$W = \cos\theta_e^{in}\,\Sigma_{ce} \quad \text{where} \quad \cos\theta_e^{in} \equiv \frac{\sin\theta_e - \sin\theta_c}{\sin\theta_i} \tag{M14}$$

Thus, the rescaled affinity contrast, W/Σ_{ce}, which is a mechanical quantity related to the adhesion free energies of the membrane segments, is equal to $\cos\theta_e^{in}$, where the intrinsic contact angle θ_e^{in} is a scale-invariant material parameter.

DATA AVAILABILITY STATEMENT

The source data underlying Figs. 1c-d, 2a-e, 3b,d-i, 4b-c as well as Supplementary Figs. 1a-f, 2a-c, 3a-c, 4a-c, 5, 6, 7a-b, 8 are provided in a separate Excel file labelled 'Source Data' with this paper.

ACKNOWLEDGEMENTS

A.M. acknowledges support from Alexander von Humboldt Foundation and CONICET. We acknowledge Nannan Chen for providing glycinin, and Clemens Schmitt for the assistance with Raman experiments. We also acknowledge support from the German Academic Exchange Service (Deutscher Akademischer Austauschdienst, DAAD) in the framework of project 57654674. R.D. acknowledges the ComeInCell network funded by the European Union's Horizon Europe research and innovation program under the Marie Skłodowska-Curie grant agreement No. 101168939. We would like to thank Dr. Leonel Malacrida for the helpful discussions regarding ACDAN hyperspectral imaging and fluorescence mechanisms.

REFERENCES

1. Decker, C.J. & Parker, R. P-bodies and stress granules: possible roles in the control of translation and mRNA degradation. *Cold Spring Harbor perspectives in biology* **4**, a012286 (2012).
2. Feric, M. et al. Coexisting Liquid Phases Underlie Nucleolar Subcompartments. *Cell* **165**, 1686-1697 (2016).
3. Feric, M. et al. Mesoscale structure–function relationships in mitochondrial transcriptional condensates. *Proceedings of the National Academy of Sciences* **119**, e2207303119 (2022).
4. Fei, J. et al. Quantitative analysis of multilayer organization of proteins and RNA in nuclear speckles at super resolution. *Journal of cell science* **130**, 4180-4192 (2017).
5. Bussi, C. et al. Stress granules plug and stabilize damaged endolysosomal membranes. *Nature* **623**, 1062-1069 (2023).
6. Alberti, S. & Hyman, A.A. Biomolecular condensates at the nexus of cellular stress, protein aggregation disease and ageing. *Nature Reviews Molecular Cell Biology* **22**, 196-213 (2021).
7. Watson, J.L. et al. Macromolecular condensation buffers intracellular water potential. *Nature* **623**, 842-852 (2023).

8. Lyon, A.S., Peeples, W.B. & Rosen, M.K. A framework for understanding the functions of biomolecular condensates across scales. *Nat Rev Mol Cell Biol* **22**, 215-235 (2021).
9. Smokers, I.B., Visser, B.S., Slootbeek, A.D., Huck, W.T. & Spruijt, E. How Droplets Can Accelerate Reactions– Coacervate Protocells as Catalytic Microcompartments. *Accounts of Chemical Research* **57**, 1885-1895 (2024).
10. Jawerth, L. et al. Protein condensates as aging Maxwell fluids. *Science* **370**, 1317-1323 (2020).
11. Ye, S. et al. Micropolarity governs the structural organization of biomolecular condensates. *Nature Chemical Biology* **20**, 443-451 (2024).
12. Alshareedah, I. et al. Sequence-specific interactions determine viscoelasticity and ageing dynamics of protein condensates. *Nature Physics* **20**, 1482-1491 (2024).
13. Abyzov, A., Blackledge, M. & Zweckstetter, M. Conformational dynamics of intrinsically disordered proteins regulate biomolecular condensate chemistry. *Chemical Reviews* **122**, 6719-6748 (2022).
14. Boeynaems, S. et al. Spontaneous driving forces give rise to protein− RNA condensates with coexisting phases and complex material properties. *Proceedings of the National Academy of Sciences* **116**, 7889-7898 (2019).
15. Joshi, A. et al. Hydrogen-Bonded Network of Water in Phase-Separated Biomolecular Condensates. *The Journal of Physical Chemistry Letters* **15**, 7724-7734 (2024).
16. Mangiarotti, A. et al. Biomolecular condensates modulate membrane lipid packing and hydration. *Nature Communications* **14**, 6081 (2023).
17. Dogra, P., Joshi, A., Majumdar, A. & Mukhopadhyay, S. Intermolecular charge-transfer modulates liquid–liquid phase separation and liquid-to-solid maturation of an intrinsically disordered pH-responsive domain. *Journal of the American Chemical Society* **141**, 20380-20389 (2019).
18. Dai, Y. et al. Interface of biomolecular condensates modulates redox reactions. *Chem* **9**, 1594-1609 (2023).
19. Zhu, L., Pan, Y., Hua, Z., Liu, Y. & Zhang, X. Ionic effect on the microenvironment of biomolecular condensates. *Journal of the American Chemical Society* **146**, 14307-14317 (2024).
20. Cui, J. et al. Mitochondria-targeted ratiometric fluorescent probes for micropolarity and microviscosity and their applications. *Chinese Chemical Letters* **30**, 1071-1074 (2019).
21. Xiao, H., Li, P. & Tang, B. Recent progresses in fluorescent probes for detection of polarity. *Coordination Chemistry Reviews* **427**, 213582 (2021).
22. Levitt, J.A., Chung, P.-H. & Suhling, K. Spectrally resolved fluorescence lifetime imaging of Nile red for measurements of intracellular polarity. *Journal of biomedical optics* **20**, 096002-096002 (2015).
23. Yang, Z. et al. A Nile Red/BODIPY-based bimodal probe sensitive to changes in the micropolarity and microviscosity of the endoplasmic reticulum. *Chemical Communications* **50**, 11672-11675 (2014).
24. Vorontsova, I. et al. In vivo macromolecular crowding is differentially modulated by aquaporin 0 in zebrafish lens: Insights from a nanoenvironment sensor and spectral imaging. *Science Advances* **8**, eabj4833 (2022).
25. Schlüßler, R. et al. Correlative all-optical quantification of mass density and mechanics of subcellular compartments with fluorescence specificity. *Elife* **11**, e68490 (2022).
26. Hong, Y. et al. Label-free quantitative analysis of Coacervates via 3D phase imaging. *Advanced Optical Materials* **9**, 2100697 (2021).
27. Linsenmeier, M. et al. Dynamic arrest and aging of biomolecular condensates are modulated by low-complexity domains, RNA and biochemical activity. *Nature Communications* **13**, 3030 (2022).
28. Zhu, L., Pan, Y., Hua, Z., Liu, Y. & Zhang, X. Ionic Effect on the Microenvironment of Biomolecular Condensates. *Journal of the American Chemical Society* (2024).
29. Wu, T. et al. Single-fluorogen imaging reveals distinct environmental and structural features of biomolecular condensates. *Nature Physics* **21**, 778-786 (2025).

30. Rodríguez, L.C., Foressi, N.N. & Celej, M.S. Tracking protein transitions through fluorescence spectral phasor analysis with ACDAN. *Biophysical Reports* **5** (2025).
31. Wang, L. et al. Xanthone-based solvatochromic fluorophores for quantifying micropolarity of protein aggregates. *Chemical Science* **13**, 12540-12549 (2022).
32. Weber, G. & Farris, F.J. Synthesis and spectral properties of a hydrophobic fluorescent probe: 6-propionyl-2-(dimethylamino) naphthalene. *Biochemistry* **18**, 3075-3078 (1979).
33. Gunther, G., Malacrida, L., Jameson, D.M., Gratton, E. & Sánchez, S.A. LAURDAN since Weber: the quest for visualizing membrane heterogeneity. *Accounts of chemical research* **54**, 976-987 (2021).
34. Thoke, H.S. et al. Tight coupling of metabolic oscillations and intracellular water dynamics in Saccharomyces cerevisiae. *PLoS One* **10**, e0117308 (2015).
35. Thoke, H.S., Thorsteinsson, S., Stock, R.P., Bagatolli, L.A. & Olsen, L.F. The dynamics of intracellular water constrains glycolytic oscillations in Saccharomyces cerevisiae. *Scientific Reports* **7**, 16250 (2017).
36. Begarani, F. et al. Capturing metabolism-dependent solvent dynamics in the lumen of a trafficking lysosome. *ACS nano* **13**, 1670-1682 (2019).
37. Bagatolli, L.A. To see or not to see: Lateral organization of biological membranes and fluorescence microscopy. *Biochimica et Biophysica Acta (BBA) - Biomembranes* **1758**, 1541-1556 (2006).
38. Patel, A. et al. ATP as a biological hydrotrope. *Science* **356**, 753-756 (2017).
39. Mangiarotti, A. et al. Lipid packing and cholesterol content regulate membrane wetting and remodeling by biomolecular condensates. *Nature Communications* **16**, 2756 (2025).
40. Lakowicz, J. Principles of fluorescence spectroscopy. *University of Maryland School of Medicine Baltimore* **132** (2006).
41. Myroshnychenko, V. & Brosseau, C. Finite-element modeling method for the prediction of the complex effective permittivity of two-phase random statistically isotropic heterostructures. *Journal of applied physics* **97** (2005).
42. Jiménez-Sánchez, A., Lei, E.K. & Kelley, S.O. A multifunctional chemical probe for the measurement of local micropolarity and microviscosity in mitochondria. *Angewandte Chemie International Edition* **57**, 8891-8895 (2018).
43. Socas, L.B.P. & Ambroggio, E.E. Linking surface tension to water polarization with a new hypothesis: The Ling-Damodaran Isotherm. *Colloids and Surfaces B: Biointerfaces* **230**, 113515 (2023).
44. Liu, Y., Agudo-Canalejo, J., Grafmüller, A., Dimova, R. & Lipowsky, R. Patterns of Flexible Nanotubes Formed by Liquid-Ordered and Liquid-Disordered Membranes. *ACS Nano* **10**, 463-474 (2016).
45. Liu, Y., Lipowsky, R. & Dimova, R. Concentration Dependence of the Interfacial Tension for Aqueous Two-Phase Polymer Solutions of Dextran and Polyethylene Glycol. *Langmuir* **28**, 3831-3839 (2012).
46. Lu, T., Hu, X., van Haren, M.H., Spruijt, E. & Huck, W.T. Structure-Property Relationships Governing Membrane-Penetrating Behaviour of Complex Coacervates. *Small* **19**, 2303138 (2023).
47. Mangiarotti, A., Chen, N., Zhao, Z., Lipowsky, R. & Dimova, R. Wetting and complex remodeling of membranes by biomolecular condensates. *Nature communications* **14**, 2809 (2023).
48. Chen, N., Zhao, Z., Wang, Y. & Dimova, R. Resolving the mechanisms of soy glycinin self-coacervation and hollow-condensate formation. *ACS Macro Letters* **9**, 1844-1852 (2020).
49. Sato, T., Niwa, H., Chiba, A. & Nozaki, R. Dynamical structure of oligo (ethylene glycol) s-water solutions studied by time domain reflectometry. *The Journal of chemical physics* **108**, 4138-4147 (1998).
50. Smolin, N., Oleinikova, A., Brovchenko, I., Geiger, A. & Winter, R. Properties of spanning water networks at protein surfaces. *The Journal of Physical Chemistry B* **109**, 10995-11005 (2005).

51. Nakasako, M. Water–protein interactions from high–resolution protein crystallography. *Philosophical Transactions of the Royal Society of London. Series B: Biological Sciences* **359**, 1191-1206 (2004).
52. Lamy, H. et al. Kinetic Study of the Esterase-like Activity of Albumin following Condensation by Macromolecular Crowding. *Biomacromolecules* **25**, 2803-2813 (2024).
53. Kunz, W., Holmberg, K. & Zemb, T. Hydrotropes. *Current Opinion in Colloid & Interface Science* **22**, 99-107 (2016).
54. Saurabh, S. et al. ATP-responsive biomolecular condensates tune bacterial kinase signaling. *Sci Adv* **8**, eabm6570 (2022).
55. Dragwidge, J.M. et al. Biomolecular condensation orchestrates clathrin-mediated endocytosis in plants. *Nature cell biology* **26**, 438-449 (2024).
56. Ma, X., Li, P. & Ge, L. Targeting of biomolecular condensates to the autophagy pathway. *Trends in Cell Biology* **33**, 505-516 (2023).
57. Li, Y., Lipowsky, R. & Dimova, R. Transition from complete to partial wetting within membrane compartments. *Journal of the American Chemical Society* **130**, 12252-12253 (2008).
58. Kumar, R., Sumpter, B.G. & Muthukumar, M. Enhanced Phase Segregation Induced by Dipolar Interactions in Polymer Blends. *Macromolecules* **47**, 6491-6502 (2014).
59. Ling, G.N. Life at the cell and below-cell level: The hidden history of a fundamental revolution in biology. (Pacific Press New York, 2001).
60. Mukherjee, S. & Schäfer, L. (2023).
61. Chen, S. & Wang, Z.-G. Driving force and pathway in polyelectrolyte complex coacervation. *Proceedings of the National Academy of Sciences* **119**, e2209975119 (2022).
62. Ylitalo, A.S., Balzer, C., Zhang, P. & Wang, Z.-G. Electrostatic correlations and temperature-dependent dielectric constant can model LCST in polyelectrolyte complex coacervation. *Macromolecules* **54**, 11326-11337 (2021).
63. Wessén, J., Pal, T., Das, S., Lin, Y.-H. & Chan, H.S. A Simple Explicit-Solvent Model of Polyampholyte Phase Behaviors and Its Ramifications for Dielectric Effects in Biomolecular Condensates. *The Journal of Physical Chemistry B* **125**, 4337-4358 (2021).
64. Workman, R.J. & Pettitt, B.M. Thermodynamic Compensation in Peptides Following Liquid–Liquid Phase Separation. *The Journal of Physical Chemistry B* **125**, 6431-6439 (2021).
65. Janssen, A.F.J. et al. Patching up the nucleus: a novel role for PMLII in nuclear envelope rupture repair. *bioRxiv*, 2025.2001.2024.634656 (2025).
66. Zimmermann, T., Rietdorf, J. & Pepperkok, R. Spectral imaging and its applications in live cell microscopy. *FEBS Lett* **546**, 87-92 (2003).
67. Patel, A. et al. A liquid-to-solid phase transition of the ALS protein FUS accelerated by disease mutation. *Cell* **162**, 1066-1077 (2015).
68. Aggarwal, S. et al. Myelin membrane assembly is driven by a phase transition of myelin basic proteins into a cohesive protein meshwork. *PLoS biology* **11**, e1001577 (2013).
69. Lipowsky, R. Response of membranes and vesicles to capillary forces arising from aqueous two-phase systems and water-in-water droplets. *The Journal of Physical Chemistry B* **122**, 3572-3586 (2018).